INTEGRAL

Science Operations Centre

Announcement of Opportunity for Observing Proposals

IBIS Observer's Manual

INTG-AO-00024

Issue 1.0

22 February 2019

Maintained by

Jan-Uwe Ness

This page was intentionally left blank

Contributors to this manual include:

(in alphabetical order)

P. Barr†, ESA-ESTEC, Noordwijk (passed away in 2005)

L. Bassani, IASF-INAF, Bologna

A. Bazzano, IASF-INAF, Rome

G. Belanger, ESA-ESAC, Madrid (maintainer)

V. Bianchin, IASF-INAF, Bologna

M. Cadolle-Bel, ESA-ESAC, Madrid (now at MPG, Germany)

I. Caballero, CEA, Saclay (now at Amadeus, Spain)

G. DiCocco, IBIS Co-PI (PICsIT) IASF-INAF, Bologna

L. Foschini, IASF-INAF, Bologna (now on Fermi Team)

A. Goldwurm, CEA, Saclay/APC, Paris

A. Gros, CEA, Saclay (now on SVOM)

D. Götz, CEA, Saclay (now on SVOM)

E. Kuulkers, ESA-ESAC, Madrid

P. Kretschmar, ESA-ESAC, Madrid

P. Laurent, IBIS Co-P.I (ISGRI), Saclay/APC, Paris

F. Lebrun, APC, Paris (now retired)

J. Lockley, University of Southampton (now at ICR, England)

F. Mattana, APC, Paris (now at OWI, France)

L. Natalucci, IASF-INAF, Rome

M. Renaud, CEA, Saclay (now at LUPM, France)

A. Sauvageon, CEA, Saclay

S. Soldi, CEA, Saclay (now at Evolution Energy, France)

R. Terrier, APC, Paris

P. Ubertini, IBIS P.I., IASF-INAF, Rome

C. Winkler, ESA-ESTEC, Noordwijk (now retired)

J. Zurita Heras, APC, Paris (now at HEPIA, Switzerland)

Table of Contents

This page was intentionally left blank

1 Introduction

IBIS (**I**mager on **B**oard the **I**NTEGRAL **S**atellite; Ubertini et al. 2003, A&A, 411, L131) is one of the two prime instruments of the INTEGRAL scientific payload. This γ-ray telescope working in the energy range from ~15 keV to several MeV, observes various celestial objects from galactic X-ray binaries and cataclysmic variables, to active galactic nuclei and clusters of galaxies. It has powerful diagnostic capabilities: fine imaging with localization of weak sources to within a few arcminutes, and good spectral sensitivity and resolution in the continuum and emission lines. These are overviewed in Table 1.

Table 1. IBIS technical specifications

Operating energy range	15 keV - 10 MeV
Continuum sensitivity[1] (ph cm^{-2} s^{-1} keV^{-1})	2.85×10^{-6} @ 100 keV 1.6×10^{-6} @ 1 MeV
Line sensitivity[2] (ph cm^{-2} s^{-1})	1.9×10^{-5} @ 100 keV 3.8×10^{-4} @ 1 MeV
Energy resolution (FWHM)	8% @ 100 keV 10% @ 1 MeV
Angular resolution (FWHM)	12'
Point source location accuracy (90% error radius)	1' for SNR = 30 (ISGRI) 3' for SNR = 10 (ISGRI) 5–10' for SNR = 10 (PICsIT)
Timing accuracy	61 μs - 1 hr
Field of view	$8.33^\circ \times 8.00^\circ$ (fully coded) $29.11^\circ \times 29.42^\circ$ (zero response)

[1] Based on in-flight measurements; 3σ detection in10^5s, ΔE=E/2

[2] For a 3σ detection in 10^6 s

Imaging is performed using a coded mask. There are two detectors operating simultaneously: the **I**ntegral **S**oft **G**amma-**R**ay **I**mager, ISGRI, a semi-conductor array optimised for lower energies (18 keV – 1 MeV), and the **PI**xellated **C**eas**I**um **I**odide (**CsI**) **T**elescope, PICsIT, a crystal scintillator for higher energies (175 keV – 10 MeV). Figure 1 shows the total effective area of the two detectors as a function of energy, where absorption by parts of the instrument above the detector plane is taken into account.

In the following sections we provide detailed descriptions of the components that make up the IBIS telescope (§2), of how the instrument works (§3), and of its overall performance (§4). Some practical examples, calculating observing times and expected detection significances, are intended to provide help to prospective observers (§5).

More details on all aspects of IBIS and INTEGRAL are found in the A&A special issue (2003, Vol. 411). More specifically, for descriptions relating to the IBIS data analysis, see Goldwurm et al. 2003 (A&A, 411, L223).

The validation reports of the **O**ff-line **S**cientific **A**nalysis (OSA) software, as well as descriptions of the data analysis modules and pipeline can be found in the *IBIS Analysis User Manual* from the ISDC web site: http://www.isdc.unige.ch

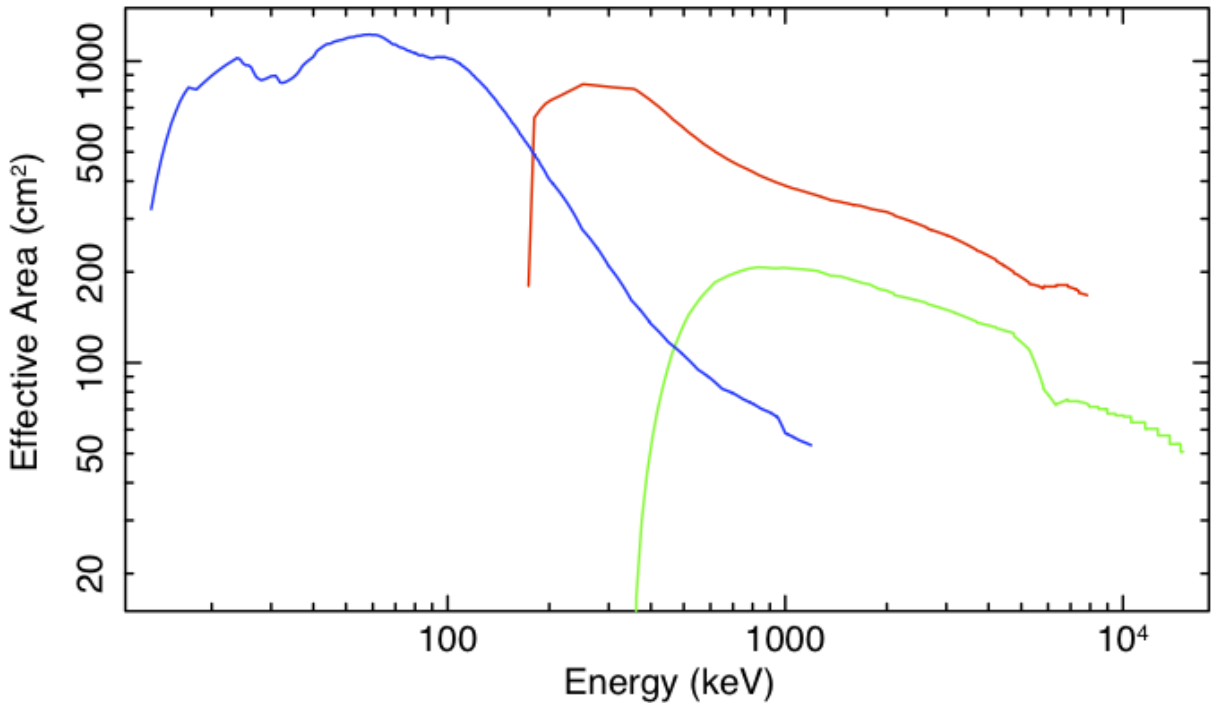

Figure 1: Ancillary response function: ISGRI (blue) and PICsIT (single: red, multiple: green).

2 Description of the instrument

2.1 The telescope

IBIS is a γ-ray imager operating in the energy range from 15 keV to 10 MeV. This range is covered by two simultaneously operating detectors located behind a Tungsten mask that provides the encoding by modulating the flux from astrophysical sources.

The coded mask is optimised for high angular resolution. As diffraction is negligible at γ-ray wavelengths, the angular resolution of a coded-mask telescope is defined by the ratio of the mask element size (11.2 mm) and the distance between the mask and the detection plane (3.2 m). It is given by: $\tan^{-1}$ (11.2/3200) = 0.2 degree or 12 arcminutes (FWHM).

The detector is composed of two pixellated detecting layers: ISGRI (Lebrun et al., 2003, A&A, 411, L141) and PICsIT (Labanti et al., 2003, A&A, 411, L149). The first is made of Cadmium-Telluride (CdTe) solid-state detectors, and the second of Cesium-Iodide (CsI) scintillator crystals. This configuration ensures a good broad continuum and line sensitivity over a wide spectral range, and allows the paths of photons to be traced in three dimensions if the event triggers both ISGRI and PICsIT within 1.9 μs. The application of Compton reconstruction algorithms to these types of events (above a few hundred keV) allows, in principle, an increase in Signal-to-Noise Ratio (SNR) by rejecting events that are unlikely to come from the source.

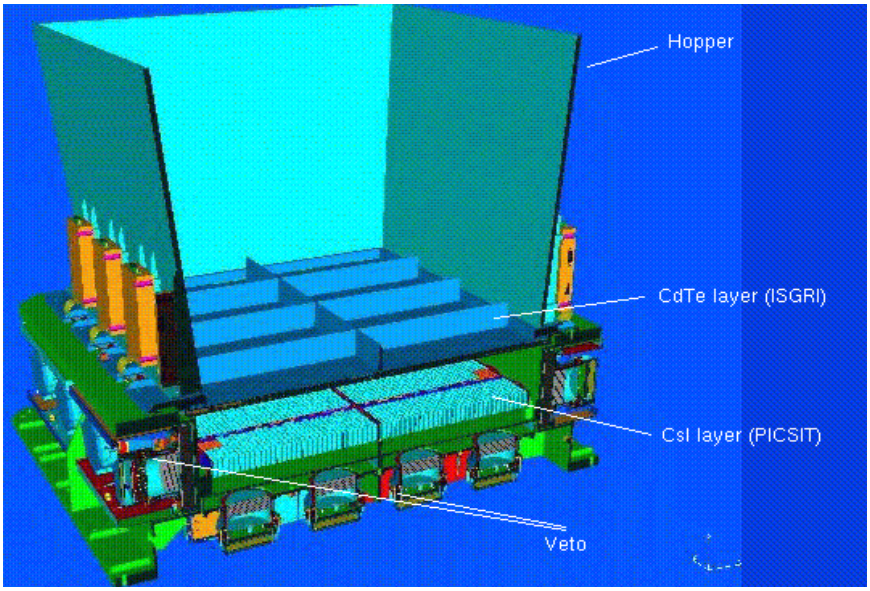

Figure 2. Cutaway drawing of the IBIS detector assembly together with the lower part of the collimator (''Hopper''). The coded mask (not shown) is located 3.2 m above the ISGRI detector

The detector aperture is restricted to the hard X-ray part of the spectrum by passive shielding covering the distance between mask and detector plane. An active Bismuth Germanate Oxide (BGO) scintillator Veto system shields the detector bottom as well as the sides of the detector, up to the bottom of ISGRI (see top of the tube walls).

2.2 The imaging system

2.2.1 Collimator

In order to maintain the low-energy response of IBIS when dithering (see *Mission Overview, Policies and Procedures*), the collimation baseline consists of a passive lateral shield that limits the solid angle, (and thus the cosmic γ-ray background), viewed directly by the IBIS detector in the full field of view up to a few hundred keV. The tube collimation system is implemented with three different devices:

Hopper: Four inclined walls starting from the detector unit with a direct interface to the IBIS detector mechanical structure. The inclination of the hopper walls should ideally be such that the area laid out by the bottom of walls matches the mask size, but the true inclination takes into account the presence of the Calibration System and the mechanical constraints. The hopper walls reach 550 mm out from the ISGRI top plane (850 mm from the PLM base) while the actual height is 530 mm. The shielding effect is obtained with Tungsten foils embedded in the four hopper walls. The hopper walls thickness is 1 mm. The hopper is not physically connected to the structure of the Payload Module (PLM).

Tube*:* The Tube is formed of four payload module walls, and shielded by lead (Pb) foil that is glued on. Two of the tube walls (± Z axis) are inclined (by about 3.5° to the vertical) in order to follow as closely as possible the inclined tube shape, whilst the Y-axis walls are vertical. In particular the actual inclination of the Z walls is defined by the interface requirements with the hopper: the Z Tube walls stop at 20 mm in the horizontal plane from each upper edge of the hopper walls, i.e., at 850 mm from the base of the PLM.

Mask side shielding: Four strips of 1 mm thick Tungsten, provide shielding from the diffuse background in the gaps between the mask edges and the top of the tube walls.

2.2.2 The mask assembly

The IBIS Mask Assembly is rectangular with external dimensions of 1180 × 1142 × 114 mm^3, and consists of three main subsystems: the Coded Mask, the Support Panel and the Peripheral Frame with the necessary interface provisions.

Coded Mask is a square of size 1064 × 1064 × 16 mm^3 made up of 95 × 95 individual square cells of size 11.2 × 11.2 mm^2. The cells form a Modified Uniformly Redundant Array (MURA) coded pattern of 53 × 53 elements (see *Figure 3*). Approximately half of the cells are opaque to photons in IBIS' operational energy range, offering 70% opacity at 1.5 MeV. The other half of the cells are "open", with an off-axis transparency of 60% at 20 keV.

Support Panel includes additional elements to support the mask, providing the necessary stiffness and strength to withstand the launch and the in-orbit operational temperatures.

Peripheral Frame reinforces the sandwich panel and provides the mechanical interfaces with the PLM.

2.3 Detector assembly

The detector layers are naturally located "under" the coded mask: ISGRI is above and PICsIT is below, separated by 9 cm.

2.3.1 Upper detector layer: ISGRI

Cadmium Telluride (CdTe) is a II-VI semi-conductor operating at an ambient temperature; 0° ± 20° C is the optimum range. As CdTe detectors can be made to have a relatively small surface, they are ideally suited to build a pixelated imager with good spatial resolution. On the other hand, their small thickness (necessary to achieve good energy resolution) restricts their use to the low energy domain (50% efficiency at 150 keV). Providing spectral performances intermediate between those attained by the cooled Germanium spectrometers (SPI) and the scintillators (PICsIT), CdTe can be used in the low energy domain down to 12 keV, and very reliably down to 18 keV for data at the beginning of the mission and down to 25 keV in 2014. The deterioration of the CdTe with time causes a loss in gain (more details in section 4.2).

The CdTe layer is made of 8 identical Modular Detection Units (MDUs; see *Figure 3*) each having 2048 pixels read out by 512 Application Specific Integrated Circuits, ASICs (4 channels per ASIC). Each MDU is connected independently to a Detector Bias Box (DBB) and to a Module Control Electronics (MCE) system that ensures the A/D conversion and provides other on-board processing such as event filtering and active pixel monitoring.

The specifications of the ISGRI layer are:

- Pixel (CdTe crystal) dimension: 4 x 4 mm^2, 2 mm thick
- Spacing between pixels: 600 μm (4.6 mm centre-to-centre)
- Minimum assembly: polycell of 16 pixels (4 x 4)
- MDU: 128 polycells (16 x 8)
- Layer: 8 MDUs (total of 8 x 64 x 32 pixels)
- Total sensitive area: 2621 cm^2 (16384 x 16 mm^2).

The CdTe layer is about 15 mm thick and is located at 294 mm above the PLM base plane.

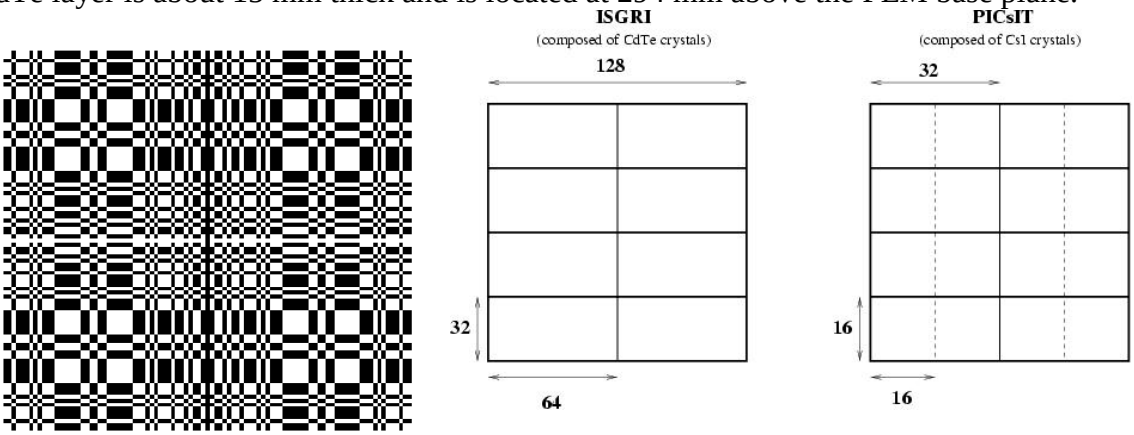

Figure 3. The IBIS coded mask model (left), and ISGRI and PICsIT detector module structure.

2.3.2 Lower detector layer: PICsIT

Caesium Iodide (CsI) is a I-VII scintillation crystal. The main characteristics of the layer are:

- Pixel (CsI) crystal dimension: 8.4 × 8.4 mm^2, 30 mm thick
- Spacing between pixels: 800 μm (9.2 mm centre-to-centre)
- Minimum assembly (ASIC): 16 pixels (4 × 4)

- Module: 32 ASICs
- Layer: 8 Modules (total of 8 × 32 × 16 pixels)
- Total sensitive area: 2994 cm^2 (4096 × 71 mm^2)

The CsI(Tl) bars are optically bonded to custom-made low-leakage silicon PIN photodiodes. The design provides a high degree of modularity. The CsI(Tl) layer is divided in 8 rectangular modules of 512 detector elements, each module being integrated into a stand-alone, testable sub-system. The CsI modules have the same cross-sectional shape as those of the CdTe (*Figure 3*).

2.4 Veto shield system

The Veto system (Quadrini et al. 2003, A&A, 411, L153) is crucial to the operations of IBIS, because it is used as part of the anti-coincidence system to discriminate against background particles and photons propagating through, or induced within the spacecraft.

The sides of the telescope up to the ISGRI bottom level and rear of the stack of detector planes are surrounded by an active BGO Veto shield. Like the detector array, the Veto shield is modular in construction. There are 8 lateral shields (2 modules per side), and 8 bottom modules. Each Veto Detector Module (VDM) includes:

- the BGO crystal and related housing
- two photomultiplier tubes (PMTs) optically coupled to the BGO and assembled with the dedicated Front End Amplifiers and High Voltage (HV) divider
- one HV Power Supply
- one Veto Module Electronics box for Module control
- internal harness

The high density and mean Z of the BGO ensure that a thickness of 20 mm is sufficient to significantly reduce the detector background (caused by leakage through the shielding of cosmic diffuse and spacecraft-induced γ-rays), to less than the sum of all other background components.

2.5 Electronics

2.5.1 Analogue Front End Electronics (AFEE)

Charge collection, signal filtering and amplification are all performed by the Application Specific Integrated Circuits (ASICs) on both ISGRI and PICsIT. In ISGRI, the 16384 individual detector units (pixels) are grouped into hybrid circuits called *polycells*, which are the basic assembly unit of a detector module, receiving a signal from 16 detectors via 4 ASICs.

2.5.2 Module Control Electronics (MCE) and PICsIT Electronic Box (PEB)

The MCE and PEB perform receipt, checking and execution of telecommands for ISGRI and PICsIT, respectively. They also collect and format the housekeeping data and process the analogue and digital data (energy and rise time). An important function of the MCE is to monitor the CdTe noise levels.

In-flight, a CdTe detector can become noisy and trigger the relevant MCE too frequently, causing a large dead time with unacceptable loss of photons. Therefore, the MCE monitors in real time the relative counting rates of each CdTe polycell. If a polycell exhibits noise, the MCE will, if necessary, switch it off. It can subsequently be reactivated and checked from the ground.

2.5.3 On-board calibration unit

After 12 years in orbit, the on-board collimated radioactive ^{22}Na calibration source has been disabled and has no more use.

2.5.4 Digital Front End Electronics (DFEE) and FIFO

The DFEE is situated behind the AFEE and processes the ASICs output for the First-In, First-Out (FIFO) data manager. FIFO sorts the events from different modules according to their true arrival time in the detector plane for transmission to the DPE/HEPI (see next section). The DFEE also monitors the FIFO and instructs it when to send data to the DPE.

2.5.5 Data Processing Electronics (DPE) and Hardware Event Processor (HEPI)

The detector electronics chain ends at the DPE and the HEPI. The HEPI performs the data histogram-ing and generates the data structures for the DPE. The DPE handles all the interfaces between the instruments and the spacecraft for both uplink and downlink. For example, it handles the packet-ing of data for the On-Board Data-Handling System before transmission to the ground.

3 How the instrument works

3.1 Detection

Photons are detected in IBIS by several methods (Figure 4):

Detection in ISGRI: a photon is stopped in a single pixel of the semi-conductor, generating an electric pulse. Each photon that penetrates a CdTe pixel in ISGRI, ionizes the material and creates electron and hole pairs. In the polarizing electric field (bias voltage), the light and negatively charged electrons travel towards the positive electrodes faster than the heavier holes moving in the opposite direction. The current created by the movement of the charges induces a pulse whose height, for a fixed depth of interaction, is directly proportional to the number of electron-hole pairs. For interactions deep in the detector the pulse height decreases due to less efficient charge collection, while pulse rise time increases. For further details see Limousin et al. 2001, NIMPR A, 471, 174.

The detector coordinates, the pulse height and the rise time of each event are stored in the form of a list (raw data) from which, through the use of two look-up tables, the deposited energy of an event can be reconstructed; the first one is used to transform the pulse height from a number of channels to an energy in keV by applying the gain correction appropriate to each pixel, while the second combines the rise time and pulse height information to determine the charge loss correction that should be applied to recover the event energy. This effect will be corrected with a time-dependent correction computed using a detailed ISGRI model in a future version of OSA.

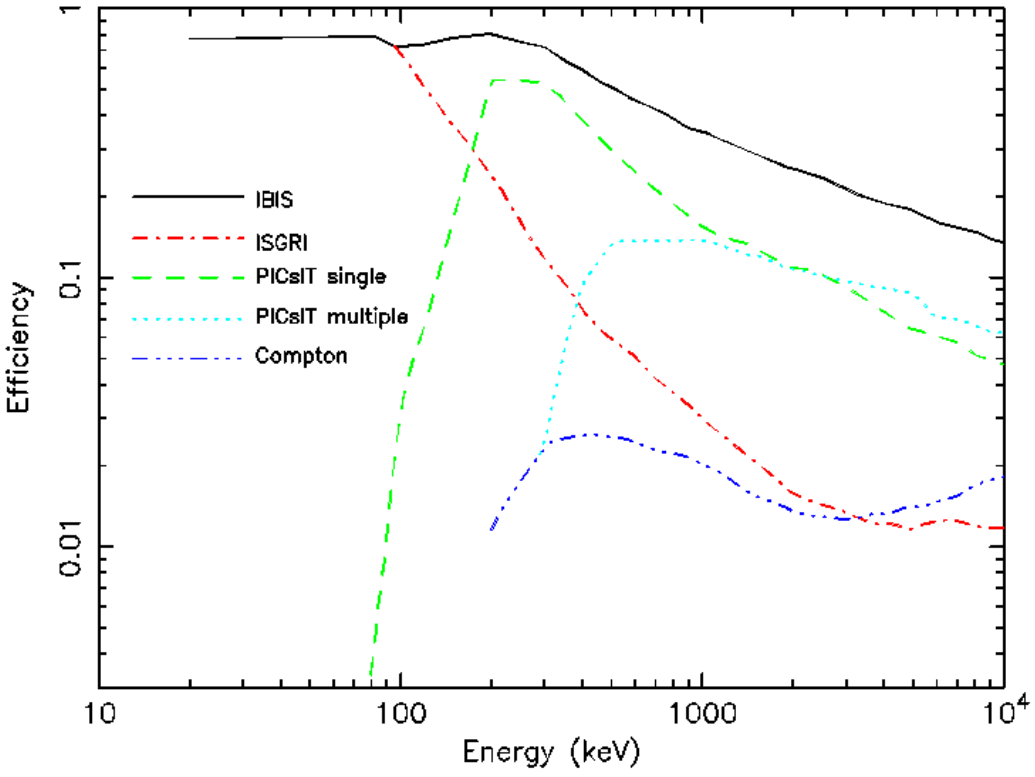

Figure 4. Detection efficiency evaluated by Monte Carlo simulation.

Detection in PICsIT: a photon passes through ISGRI and is stopped in PICsIT, generating one or more scintillation flashes. PICsIT distinguishes detections that occur in only one pixel (single events), from those that occur in more than one (multiple events).

The energy of the incident photon is derived in each crystal bar from the intensity of the flash recorded in the photodiode. For multiple events, it is derived by summing the energies derived from the intensity of each of the flashes. The energy resolution of PICsIT is a function of the SNR of the events, the electronic noise at low energies and the light output.

Detection in both ISGRI and PICSIT (Compton mode): Photons that interact in either ISGRI or PICsIT may undergo a Compton scattering, and be subsequently detected in the other layer. The energy of Compton events is determined from the sum of energies for the initial event and the photon scatter angle. (Data analysis in this mode is not supported.)

3.2 Imaging

IBIS has a field of view of 29×29 degrees (Full Width at Zero Response). A source contained within this field of view will cast a shadow of the mask onto the detector planes. However, given the geometry of the mask and hopper assembly, only for sources within the central 8°×8° around the pointing direction the detector is completely illuminated by a section of the mask; this defines the Fully Coded Field Of View (FCFOV), whereas the rest of the FOV is called Partially Coded Field Of View (PCFOV).

Since all sources present in the PCFOV contribute to the total detected flux, cross-correlation techniques are used to reconstruct the most probable configuration and intensity of the individual sources contributing to this flux.

The portion of the sky surveyed during an observation depends on the dither pattern. For the standard 5°×5° dither, the central 17°×17° are always fully coded, and a region spanning about 38°×38° is surveyed to zero response.

3.3 Timing

The ISGRI time resolution is 61.035 μs for each detected event. PICsIT spectra and images are accumulated every 1800–3600 seconds depending on dithering time; a spectrum alone (but with low resolution, from two to eight energy bands) is available every several ms.

3.4 Polarimetry

Multiple events in adjacent PICsIT cells can be used to determine the polarisation of the incident photons using the Klein-Nishina cross-section dependence on polarisation angle. However, this requires the Polarimetric sub-mode, which is never used because it was not possible to install a polarised calibration source on board (due to a lack of time and resources).

It is also possible to use the ISGRI and PICsIT detector planes in conjunction in order to select Compton events, allowing a reconstruction of the incident photon's polarisation (see Forot et al. 2008 for more details). Although there is currently no support for Compton analysis in OSA, the list of Compton events per science window are distributed together with the ISGRI and PICSIT events.

3.5 Observing modes

IBIS has several observing modes for engineering and calibration purposes, but only one for scientific observations. In *science mode*, there are no user-selectable parameters, and ISGRI registers and transmits photon-by-photon: every event is tagged with its arrival time, energy, and position on the detector plane.

PICsIT can also operate in *photon-by-photon mode* (PPM), but because of its much higher background due to cosmic ray induced events, the limited telemetry does not allow operating in this mode because it would lead to important data losses. For this reason, the standard mode for PICsIT is *histogram mode*: registered events are integrated over the pointing duration (spectral imaging) or over the detector plane (spectral timing). Note that transmission of PPM events was disabled early in the mission, and permanently disabled at the end of revolution 1507.

For the spectral timing data, both the time resolution that ranges between 0.976 and 500 ms, and the number of energy channels can be set from the ground. Currently, PICsIT uses a time resolution of 15.625 ms and 8 energy channels: 208–260, 260–312, 312–364, 364–468, 468–572, 572–780, 780–1196 and 1196–2600 keV. The characteristics of the different observing modes for IBIS are summarized in Table 2.

Table 2: ISGRI and PICsIT observing modes

	Observing Mode	Imaging resolution (pixels)	Timing resolution	Spectral resolution (channels)
ISGRI	photon-by-photon	128x128	61.035 µs	2048
PICsIT	photon-by-photon	64x64	64 µs	1024
	spectral-imaging	64x64	30-60 min	256
	spectral-timing	none	1-500 ms	2-8

4 Performance of the instrument

4.1 Components and sources of instrumental background

The bulk of the detected photons in both ISGRI and PICsIT are not from the scientific targets that are observed. These background photons are of two types: instrumental and astrophysical, and their main sources are:

- for ISGRI at low energies (< 100 keV): cosmic-ray induced fluorescence of the shielding elements, and diffuse cosmic γ-ray background
- for ISGRI at higher energies and for PICsIT: radioactive decay of unstable nuclei created by the spallation interactions of cosmic-ray protons and their secondary particles in the massive parts of the satellite

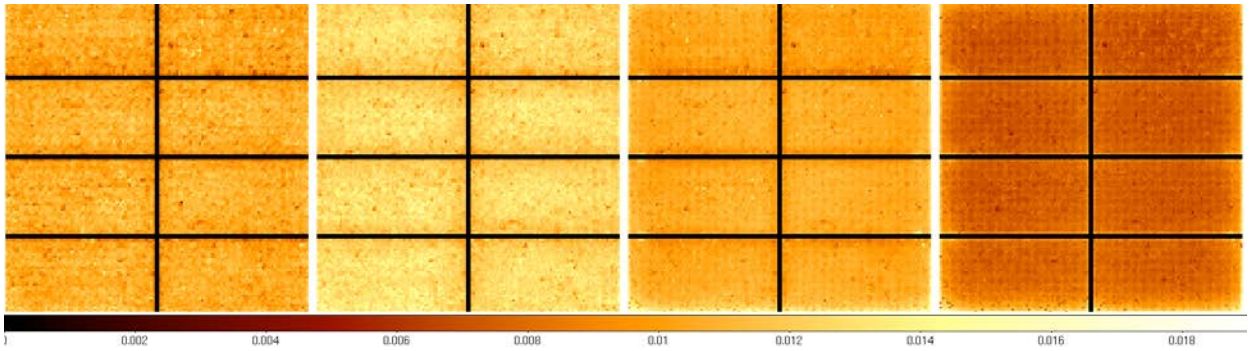

Figure 5. ISGRI time-averages intensity background maps in four logarithmically sized energy bands: 20-35, 35-60, 60-100 and 100-175 keV. The colour intensity ranges from 0 to 0.018 cps, but the maps are re-normalized depending on the count rate in each science window.

The overall background is strongly influenced by solar activity: it is lowest at solar maximum, when a stronger solar magnetic field inhibits the propagation of cosmic rays into the inner solar system, and is about twice as high at solar minimum. Veto performance is another major influence on background levels. During the Performance Verification Phase, it was found that the Veto can help to reduce the count rate by approximately 50% for ISGRI and 40% for PICsIT.

Since the background is strongly energy-dependent below ~100 keV, background cubes (2D-images as a function of energy) are constructed from all available empty fields and high latitude observations for each ISGRI energy channel (~0.5 keV). These are used by default in OSA, both for imaging and spectral analysis: the high-resolution maps are combined to match the specified energy bands. An example of these background maps is shown in Figure 5.

From the first instrument activation, bursts in the PICsIT count rate were observed (see Figure 6). In the time-integrated detector images, they are seen as tracks of bright pixels, indicating that these events are related to the interaction of cosmic rays with the detector. The contribution of these cosmic-ray induced triggers to the total PICsIT background is of the order of 10%, but they mainly affect the low-energy channels below ~300 keV (up to about 30% of the total background). Since in the standard observing mode only histograms are downloaded, this introduces non-statistical fluctuations in the data, up to a factor of a ~2.5 in the SNR.

Time-averaged, in-flight background spectra as observed by ISGRI and PICsIT are shown in Figure 7. The in-flight count rates are compared to those of the Crab in

Table ***3***.

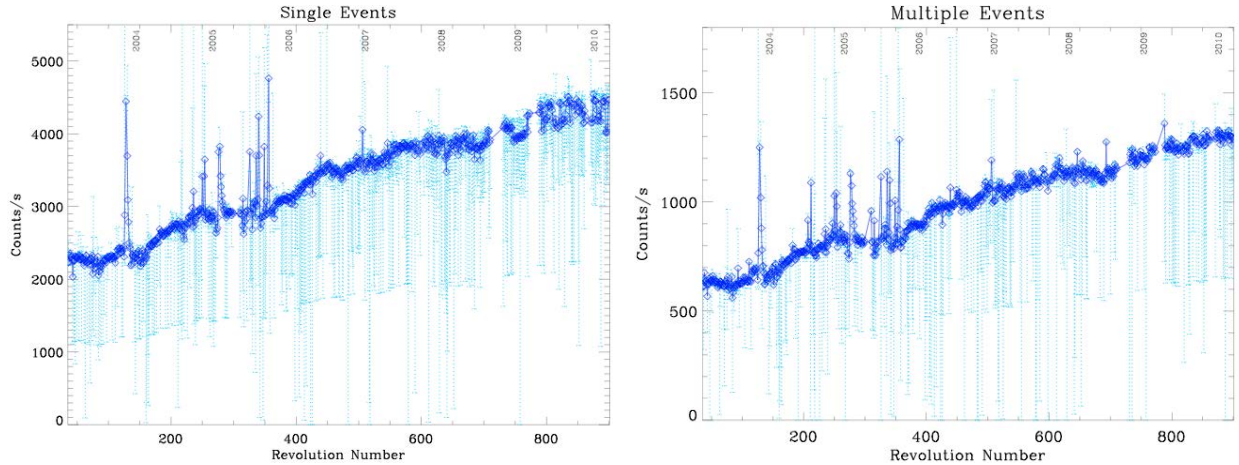

Figure 6: Total PICsIT count rate as a function of time (revolution number) at the science window level, for single (left) and multiple events (right).

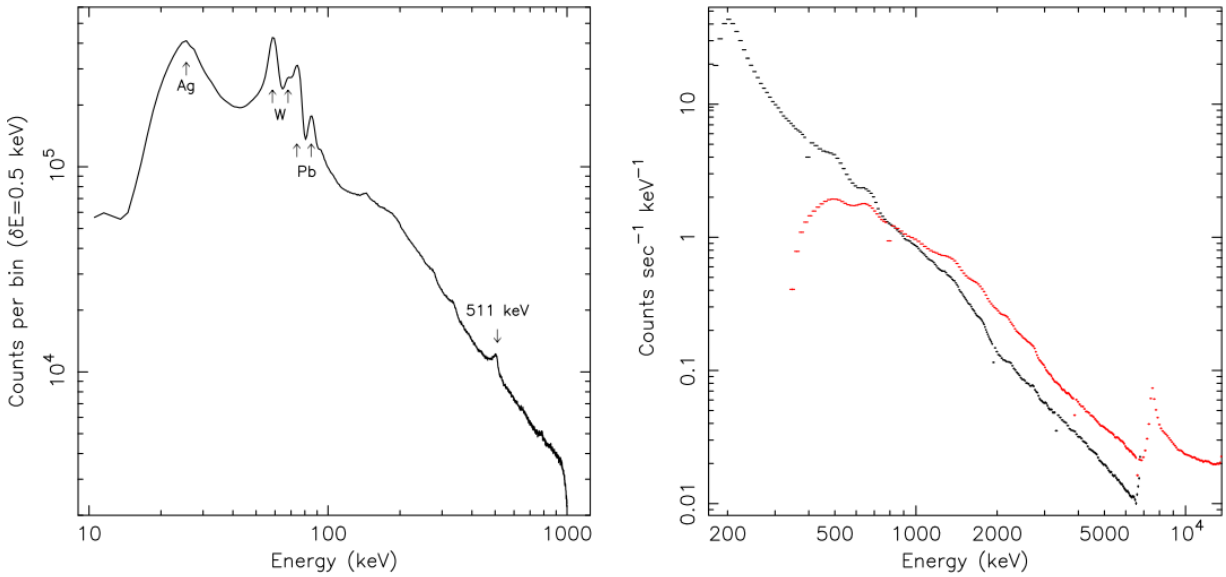

Figure 7. In-flight background spectra for ISGRI (left) and PICsIT (right). The ISGRI spectrum is from empty field observations in revolution 96 (effective exposure time 36.4 ks). For PICsIT the single (black) and multiple (red) events contributions to the background are shown separately; based on one Science Window of data accumulated in revolution 500.

Table 3. Approximate background rates compared to the Crab

Energy band	Background (Solar Max) cts s^{-1}	Crab on-axis cts s^{-1}	
ISGRI: 15-400 keV	600	250	
PICsIT:		single	multiple
203-252 keV	–	2.71±0.02	–
252-336 keV	–	2.46±0.01	–
336-448 keV	–	1.17±0.01	0.07±0.01
448-672 keV	–	0.60±0.01	0.14±0.01
672-1036 keV	–	0.26±0.01	0.14±0.01
1036-1848 keV	–	0.06±0.01	0.12±0.01
(203-1036 keV; single)	2500	7.20±0.03	–
(336-1848 keV; multiple)	580	–	0.47±0.02

IBIS is located next to SPI and JEM-X, both also coded-mask telescopes. Since γ-rays are highly penetrating, it is possible for them to pass through parts of the spacecraft or instrument structures, as well as coded masks, and to be detected by the γ-ray instruments. Therefore, off-axis γ-rays with energies above ~300 keV that pass through either the SPI or the JEM-X coded masks may cast a shadow of this mask onto the IBIS detectors; the former combination is often referred to as the ''SPIBIS'' effect (see Figure 8). Although this effectively increases the field of view of IBIS, a bright γ-ray source would thus add additional counts and modulation to the IBIS histogram, which considerably complicates the image reconstruction.

The SPIBIS effect was calibrated before launch, but ISOC avoids scheduling observations when either of the three brightest sources/regions: the Crab, Cyg X-1 or the Galactic Center region, are visible by IBIS through the SPI mask.

4.2 Instrumental characterisation and calibration

The ISGRI and PICsIT detectors are calibrated in-orbit on a regular basis. Biannual observations of the Crab are performed to enable regular verification of the detector uniformity and energy response, and improve the calibration. Continued efforts to improve our understanding of the instruments and the mask assembly allow for a steady refinement of the analysis software. At present the calibration is good up to a level of a few percent for ISGRI, and about 5% for PICsIT at off-axis angles less than ~10°. This means that in the spectral fits the deviations between the observed spectrum and actual model are generally within 2-5%.

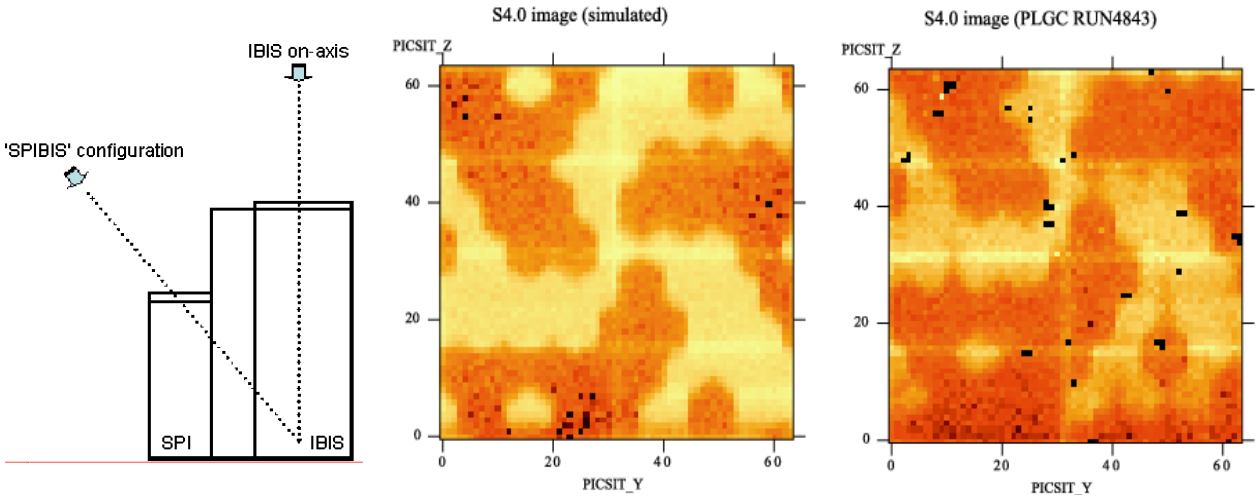

Figure 8: Left: Off-axis source positions for the SPIBIS configuration as well as the shielding tests, during the pre-flight calibrations. Middle and right: PICsIT shadowgrams from simulations (middle) and pre-flight calibration data (right). The images are slighhtly offset due to the inaccuracy in the supplied source position.

The instrument characteristics are verified after events such as solar flares. The energy response and spectral resolution are monitored on long time-scales at 59.3 keV using the background-induced Tungsten fluorescence line from the coded mask and hopper walls.

ISGRI shows a loss of gain of about 3% per year, and additional gain drops (0.6-1%) occurred after strong solar flares. Therefore, the data analysis software contains a time-dependent gain correction for ISGRI. Variations due to global temperature changes (~5°) are taken into account with an accuracy of 0.5%.

In OSA 9, the description of the gain drift is based on IREM counters integrated over time, to take into account the solar flares. However, with this correction, a clear departure from stability was seen in later data. Hence, a new gain drift correction was implemented in OSA 10.

Taking into account the expected PICsIT gain variation of 0.3% $°C^{-1}$ measured during on-ground thermal tests, the average gain (over the whole detection plane) measured in-flight indicates that the PICsIT temperature gradient along the INTEGRAL orbit is the dominant factor in the observed PICsIT gain variation. The number of disabled pixels in ISGRI is slowly increasing by about 50 per year (from 500 in 2008 to 800 in 2014; of 16384 pixels). In PICsIT there are about 50 (of 4096 pixels).

At high energies (>1 MeV), the background so strongly dominates the flux that large amounts of data accumulated through routine operations are used to extend the calibration into this regime.

In 2010, several high-energy missions detected a significant decrease in the flux from the Crab nebula that, in fact, appeared to have been steadily decreasing since 2008 (Wilson-Hodge et al. 2011). Figure 9 shows a light curve of the Crab nebula using only on-axis observations.

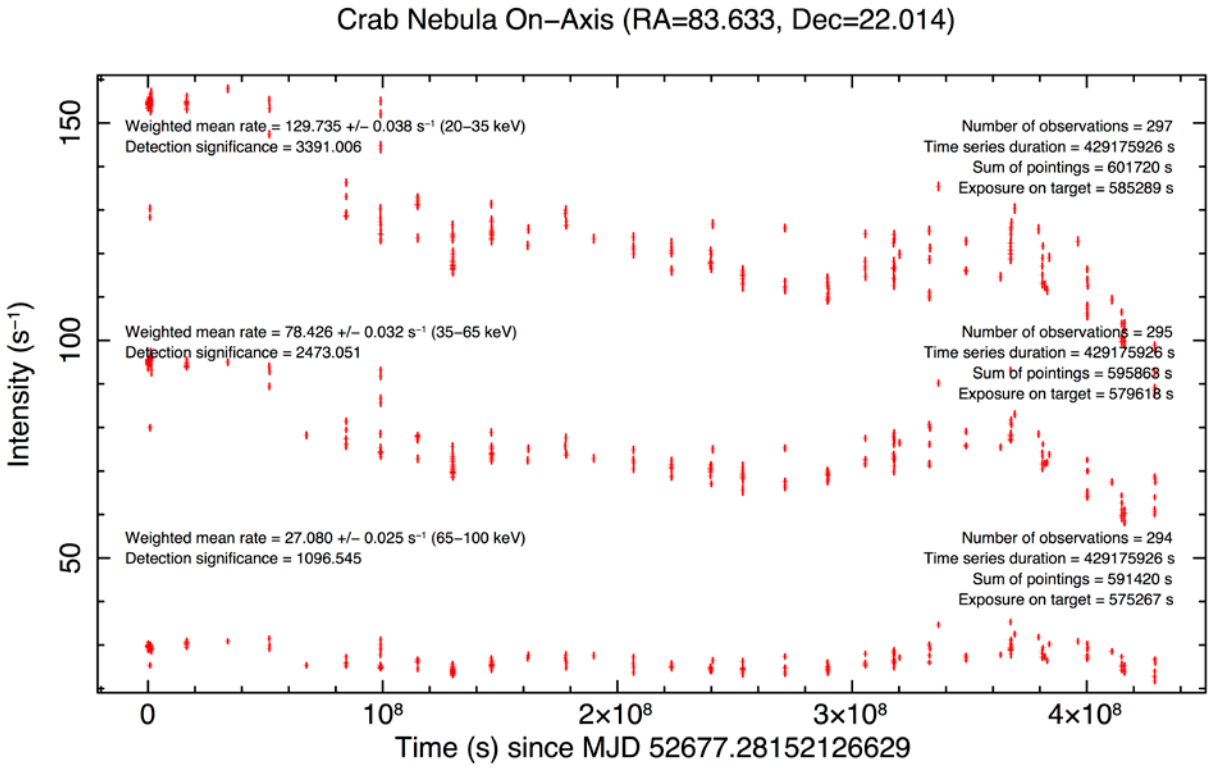

Figure 9: OSA 10.2 Crab Nebula count rate time series on-axis (within 30") in three energy bands: 20–35, 35-65, and 65-100 keV, from the start of the mission to January 2017. Each point is the estimated count rate based on a single pointing, and thus averaged over 30 to 60 minutes.

4.3 Measured performance

4.3.1 Angular resolution and point source location accuracy

The angular resolution of IBIS is 12' FWHM. However, a feature of coded masks is that the centroiding accuracy for a point source can be much finer, depending solely on the detection significance. For ISGRI, the absolute localisation accuracy for sources detected with a significance of 100 in the FCFOV is as low as 20". For a detection significance of 10, the localisation radius increases to about 2'. For PICsIT, the PSLA is roughly two times coarser.

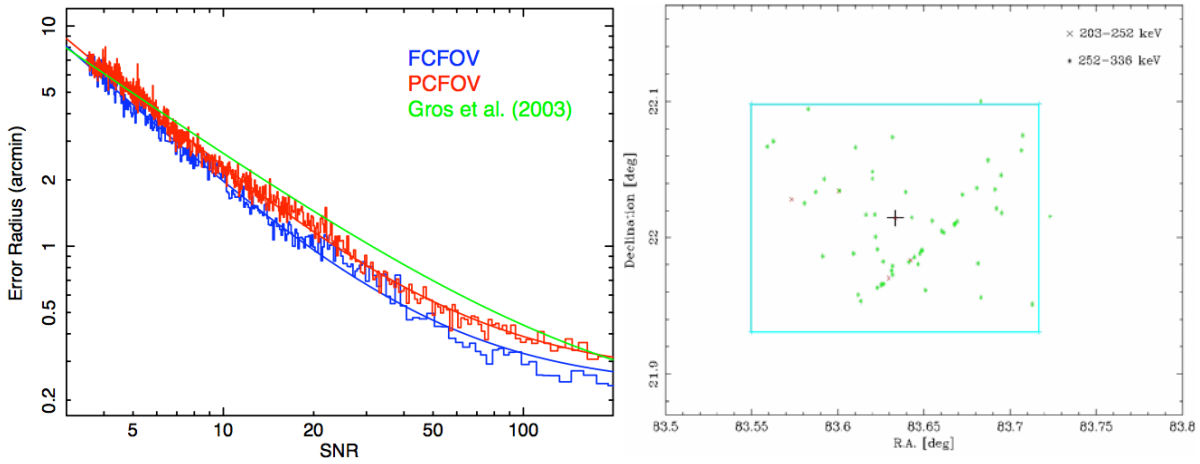

Figure 10: Left panel: ISGRI point source location accuracy (PSLA; 90% confidence level) in units of arc minutes for sources in the FCFOV using an analysis based on ~40000 science windows is given by: $31.1(SNR)^{-1.25} + 0.23$ (Scaringi et al. 2010, A&A, 516, 75). The resulting fits are shown for the FCFOV (blue) and the PCFOV (red), and are compared with the only previous determination of the PSLA by Gros et al. (2003, A&A, 141, L179), that parametrised their fit as: $22.1(SNR)^{-0.95} + 0.16$. Right panel: PICsIT PSLA using Crab observations from revolutions 39, 43, 44 and 45. Results for 2 energy bands are given (203-252 keV and 252-336 keV). Only detections with at least 3σ in a science window (or exposure) are used. The catalogue position of the Crab is marked by a cross, and the size of a PICsIT pixel (10') is indicated by the rectangle.

4.3.2 Spectral resolution

The spectral resolution of ISGRI has been measured during pre-flight tests on the engineering model, as well as in-flight. Resolutions of 9% at 60 keV (W fluorescence) and 4.6% at 511 keV have been measured from early in-flight spectra (17% at 60 keV in 2014). Figure 11 shows the earlier spectral resolution determined in-flight.

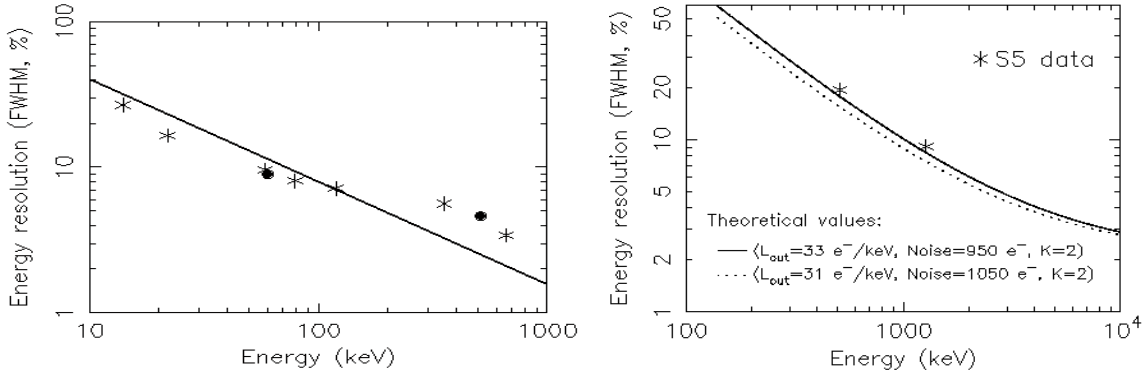

Figure 11. Left panel: The energy resolution of ISGRI. The solid line shows the theoretically expected values, and the stars are values measured before launch using an engineering model. The study of the in-flight W fluorescence line at 60 keV and the e^+/e^- annihilation lines at 511 keV (shown as filled circles) do not reveal any evidence of a change of the ISGRI spectral performance. Right panel: The energy resolution of PICsIT at 511 and 1275 keV as measured in-flight using Calibration Unit (S5) data (shown as stars). Also shown are the theoretical expectations as determined from pre-flight tests using an engineering model. The electronic-noise values ("Noise") refer to one ASIC only; a 10% increase is expected when extrapolating to the complete detector electronic chain.

4.3.3 Mask Calibration

Details such as the presence of screws, and of the amount of glue in various places on the mask, can have significant effects on the image reconstruction. This is due to the fact that the model of the mask used in the software differs from the actual mask. In order to construct a realistic model of the mask from actual observations, much effort has gone into mask calibration.

Starting with version 9.0 of OSA, improvements of the IBIS/ISGRI imaging software have been made by taking into account the presence and exact location of the screws, inserts and glue used to hold the mask in place. This is done by excluding ich these defects are projected by a bright source in the field of view. This operation yields a seven-fold improvement in sensitivity around bright sources, which, in turn, allows for the detection of much fainter sources (see Figure 12).

Even better results will be obtained by taking into account the precise shape, size and thickness of the mask defects; this is the aim of the mask calibration efforts. The goal is to measure the actual a 3D geometrical model of the mask. The empirically accurate model of the mask would then be used in the deconvolution process, further refining the image analysis software. This objective requires a uniform, effective exposure of 1 Ms over the entire mask, and dedicated observations of the Crab, together with scientific observations of the Cygnus region, are used to attain it.

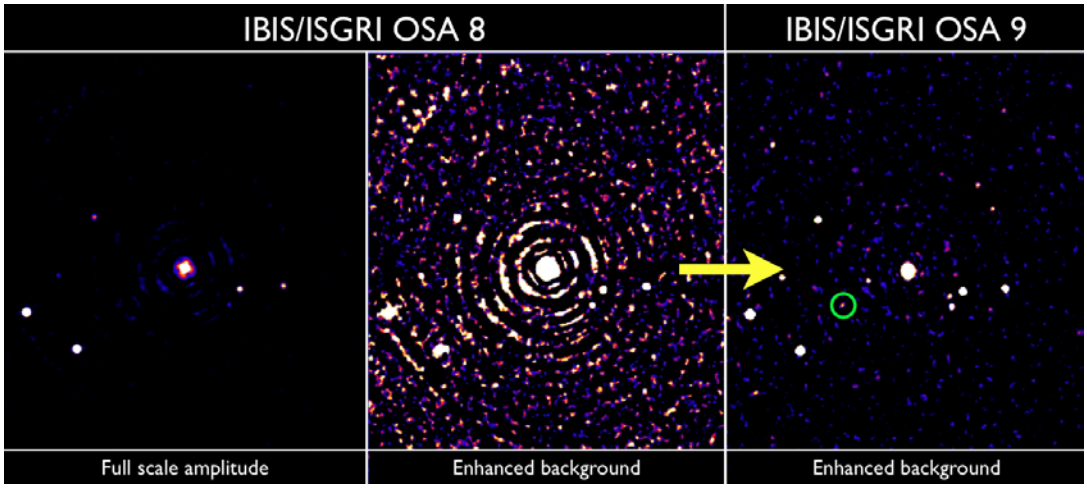

Figure 12: IBIS/ISGRI significance images of a field centred on Cyg X-1. OSA 8, standard colour scale (left), OSA 8 with a colour scale saturated to show the ghost residuals (centre) and OSA 9 with the same scale as the central image (right).

4.3.4 Off-axis response

The off-axis response of the IBIS telescope has been characterized during the Crab calibration observations in 2004, 2005 and 2006: the flux of off-axis sources could be underestimated by up to 50% in the PCFOV at energies around 20 keV. This loss is linked to the mask supporting structure (including the nomex structure), and strongly depends on the angle and the energy of the incoming radiation. The correction maps used in the imaging and spectral analysis software are shown in *Figure* 13; the residual off-axis effects after correction are less than a few percent.

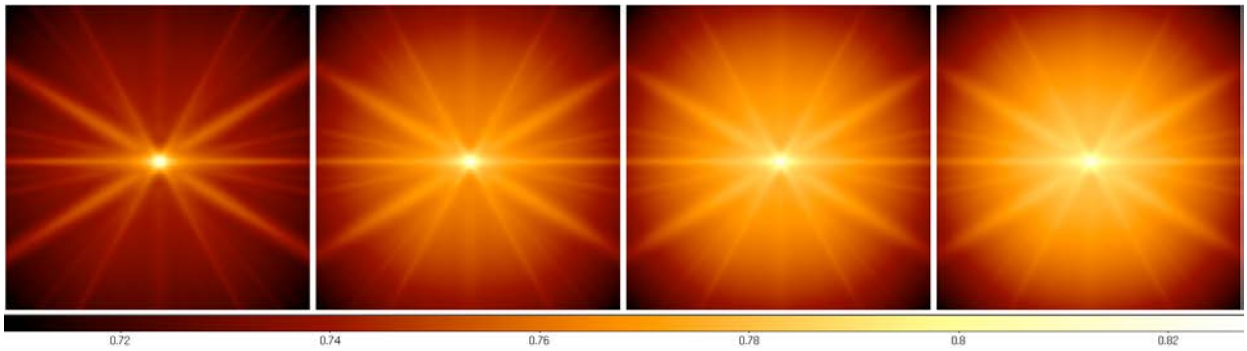

Figure 13: Off-axis correction maps based on a detailed nomex geometrical model in the energy bands 20-35, 35-60, 60-100 and 100-175 keV. In these new maps, there is an important non-axi-symmetric component characterized by the star-like shape, which is due to the hexagonal honeycomb structure of the nomex. Since these maps are used to correct the count rate, they are normalized to 1. In this example, the colour bar scale ranges from 0.71 to 0.83.

4.3.5 Sensitivity

The IBIS sensitivity can be parametrised as follows:

$$S = [n^2(\vartheta_o+\vartheta_c) + n\ sqrt[(n(\vartheta_o+\vartheta_c))^2 +4AB(\vartheta_o-\vartheta_c)^2 T\Delta E]] / [A(\vartheta_o-\vartheta_c)^2 T\Delta E\ \varepsilon]$$

In the case of the continuum, the sensitivity is measured in *photons* $cm^{-2}\ s^{-1}\ keV^{-1}$, the efficiency (the last term in the equation) is given by $\varepsilon=\varepsilon_I\varepsilon_T$, and the variable ΔE is the energy bin size. The line sensitivity is measured in *photons* $cm^{-2}\ s^{-1}$, the efficiency is $\varepsilon=\varepsilon_p$, and the variable ΔE is the energy resolution. All other variables in the equation above (in order of appearance) are defined below:

- n is the detection significance in units of sigma
- ϑ_o, ϑ_c are the open and closed mask element transparencies
- T is the observation duration
- A is the detector area
- B is the background count rate in *counts* $cm^{-2}\ s^{-1}\ keV^{-1}$
- ε_I is the imaging efficiency, a function of the coding noise and dither pattern
- ε_p, ε_T are the peak and total efficiencies, respectively

Note that for a broad line with a FWHM of ΔE keV, the sensitivity is reduced by $(\Delta E/\delta E)^{1/2}$: the square root of the ratio of the energy bin size to the energy resolution.

Figure 14 shows the sensitivity curves derived from empty field observations, and Tables 4 to 7 give some of the actual values. Theoretical agree with the observed sensitivities within a factor of ~2. This difference is due to systematic effects that increase partly due to long observations (>500 ks), and partly due to a large number of sources (this only at low energies).

Using the standard 5 × 5 dither pattern causes a slight (~2%) loss in overall sensitivity, averaged over the dither pattern, but an important imaging advantage in smoothing out systematic effects. This mode is recommended for all observations except under special circumstances that should be well motivated and justified.

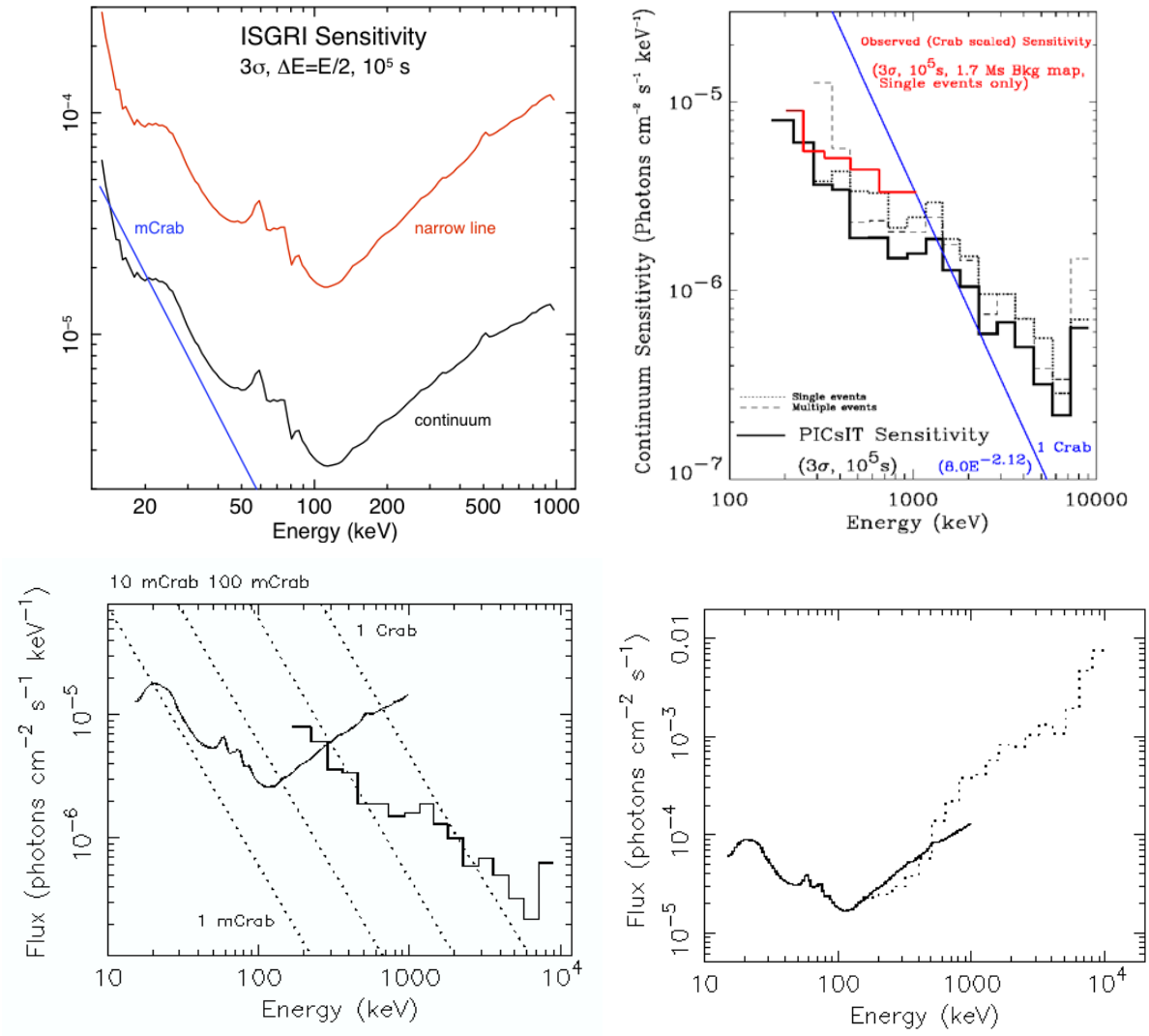

Figure 14: ***Top Left****: ISGRI continuum (black: ph cm^{-2} s^{-1} keV^{-1}) and narrow line sensitivity (red: ph cm^{-2} s^{-1}) derived from 77 ks of empty field observations.* ***Top Right****: PICsIT statistically limited continuum sensitivity is given by the black histograms, from single events (dotted), multiple events (dashed), and combined (solid), all scaled to the in-flight background count rate, and compared with the sensitivity obtained by scaling from the Crab observation (red; single events only).* ***Bottom panels****: IBIS broadband sensitivity derived from empty field observations for a 3σ detection in 10^5 s for a continuum source (ΔE = E/2; left) and a narrow line (right). Systematic uncertainties (e.g., uniformity) are not taken into account. ISGRI covers 15–1000 keV and PICsIT 200–10^4 keV (single and multiple). Reference flux is for a power-law with spectral index Γ=-2.*

Table 4. ISGRI continuum sensitivities for an on-axis source

Energy (keV)	Measured SNR (1)	Expected Crab flux (2) (ph cm^{-2} $s^{-1}$$keV^{-1}$)	Measured sensitivity (3) (ph cm^{-2} s^{-1} keV^{-1})	Statistically limited sensitivity (AO5) (3) (ph cm^{-2} s^{-1} keV^{-1})	Ratio (meas./AO5)
20–40	1149	$17.9x10^{-2}$	$27.8x10^{-6}$	$10.39x10^{-6}$	2.6
40–100	727	$10.2x10^{-2}$	$9.4x10^{-6}$	$5.02x10^{-6}$	1.9
100–200	196	$3.0x10^{-2}$	$5.2x10^{-6}$	$3.12x10^{-6}$	1.7

(1): Derived from 94.7 ks of Crab observations performed in Revolution 728, using OSA 9 with default parameters, except for OBS1_PixSpread=0 and OBS1_SearchMode=3. (see IBIS/ISGRI Validation Report available from the ISDC at http://www.isdc.unige.ch).

(2): Using a broken power-law with photon indices 2.07 and 2.24, below and above 100 keV, respectively. The flux at 1 keV is 9 ph cm^{-2} s^{-1} keV^{-1} (Jourdain et Roques 2009, ApJ, 704, 17)

(3): Sensitivities for an exposure of 100 ks, $\Delta E=E/2$, 3σ at 30, 70 and 150 keV. The different data set and spectral model prevent a straightforward comparison between the reported in the earlier versions of this document.

Table 5. ISGRI continuum sensitivities
(10^5 s exposure, 3σ detection, $\Delta E=E/2$)

Energy (keV)	ph cm^{-2} s^{-1} keV^{-1}	Energy (keV)	ph cm^{-2} s^{-1} keV^{-1}	Energy (keV)	ph cm^{-2} s^{-1} keV^{-1}
15	12.8×10^{-6}	60	6.36×10^{-6}	300	6.02×10^{-6}
20	18.0×10^{-6}	70	5.02×10^{-6}	350	6.90×10^{-6}
25	16.0×10^{-6}	80	3.94×10^{-6}	400	7.56×10^{-6}
30	10.4×10^{-6}	90	3.46×10^{-6}	450	8.41×10^{-6}
35	7.54×10^{-6}	100	2.85×10^{-6}	500	9.83×10^{-6}
40	6.16×10^{-6}	150	3.12×10^{-6}	600	10.6×10^{-6}
45	5.59×10^{-6}	200	4.10×10^{-6}	700	11.6×10^{-6}
50	5.40×10^{-6}	250	5.03×10^{-6}	800	12.7×10^{-6}

Table 6. PICsIT continuum sensitivities
(10^5 s, 3σ, $\Delta E=E/2$; single and multiple events)

Start energy (keV)	End energy (keV)	ph cm^{-2} s^{-1} keV^{-1}	Start energy (keV)	End energy (keV)	ph cm^{-2} s^{-1} keV^{-1}
170	220	7.99×10^{-6}	1200	1400	1.88×10^{-6}
220	280	6.06×10^{-6}	1400	1800	1.28×10^{-6}
280	370	3.62×10^{-6}	1800	2200	1.05×10^{-6}
370	430	3.41×10^{-6}	2200	2900	0.59×10^{-6}
430	580	1.90×10^{-6}	2900	3500	0.68×10^{-6}
580	720	1.91×10^{-6}	3500	4500	0.50×10^{-6}
720	900	1.48×10^{-6}	4500	5700	0.32×10^{-6}
900	1200	1.57×10^{-6}	5700	7100	0.22×10^{-6}

Table 7. ISGRI and PICsIT narrow line sensitivity (10^6 s, 3σ detection)

Energy (keV)	ISGRI line ph $cm^{-2}s^{-1}$	PICsIT line ph $cm^{-2}s^{-1}$	Energy (keV)	ISGRI line ph $cm^{-2}s^{-1}$	PICsIT line ph $cm^{-2}s^{-1}$
22.5	8.76×10^{-5}		566.1	8.40×10^{-5}	14×10^{-5}
28.4	6.28×10^{-5}		712.6	9.88×10^{-5}	22×10^{-5}
35.7	3.92×10^{-5}		897.2	11.9×10^{-5}	38×10^{-5}
45.0	3.13×10^{-5}		1129.5		$41x\ 10^{-5}$
56.6	3.71×10^{-5}		1421.9		57×10^{-5}
71.3	3.08×10^{-5}		1790.1		82×10^{-5}
89.7	2.17×10^{-5}		2253.6		79×10^{-5}
112.9	1.67×10^{-5}		2837.1		100×10^{-5}
142.2	1.98×10^{-5}		3571.7		$130x\ 10^{-5}$
179.0	2.54×10^{-5}	2.3×10^{-5}	4496.5		110×10^{-5}
225.4	3.21×10^{-5}	2.5×10^{-5}	5660.7		200×10^{-5}
283.7	4.27×10^{-5}	3.0×10^{-5}	7126.5		470×10^{-5}
357.2	5.31×10^{-5}	3.8×10^{-5}	8971.6		760×10^{-5}
449.6	6.64×10^{-5}	5.7×10^{-5}			

4.3.6
4.3.7 Timing

The *time resolution* in ISGRI is 61.035 μs. For PICsIT, imaging and spectral histograms are collected every 1800–3600 s, depending on the dithering time, which defines the time resolution. The spectral timing data of PICsIT (without imaging) is recorded every few ms. The default resolution is 15.625 ms, but can take a value between 0.976 and 500 ms.

The *absolute timing accuracy*, the barycentric correction to event times measured in IBIS, depends on the uncertainty in the spacecraft position, and on the time resolution and time frame synchronisation in the instrument and spacecraft subsystems. Calculations give an accuracy of 61 μs within 1σ, and 92 μs within 3σ. In-flight measurements show that the relative timing between instruments is within 10 μs, whereas the absolute timing accuracy is about 40 μs. A more accurate calibration might be performed via dedicated millisecond pulsar observations.

A detailed analysis based on the pulse profile analysis of the accretion powered pulsar (245 Hz) IGR J17511-3057 comparing the absolute timing abilities of ISGRI and RXTE's HEXTE and PCA, shows that measurements with these three instruments are consistent with each other at the level of 50 μs (Lucien Kuiper, private communication).

We distinguish between the instrument's actual detection efficiency, and the delay or instrumental dead time that follows each detected event and during which another event cannot be recorded. The BGO shielding, calibration source, and Compton coding induce additional dead times due to good events that happen to occur during their respective time windows.

In ISGRI dead time is around 25%, and is due to the combined effects of:

- Detected ISGRI events (115 μs each)
- VETO strobe length (ISGRI: 5 μs, PICsIT: 2 μs)
- Calibration source (negligible)
- Compton coincidence window for each PICsIT detection (3.8 μs per window; negligible)

PICsIT dead time is about 5%. For additional details, see the latest version of the IBIS Analysis.

5 Observation "Cook book"

In this section, there are examples on how to calculate the observation time required to attain various scientific aims. For a panoramic view of the science that can be done with INTEGRAL, browse the *Mission Overview* section of the INTEGRAL web site at the following URL: http://www.cosmos.esa.int/web/integral.

5.1 How to calculate observing times

The approximate signal-to-noise ratio (SNR) for a given exposure can be calculated from the sensitivity curves. As shown in §1.1.1, the continuum sensitivity, S_{cont}, scales with SNR, $t^{-1/2}$, and $\Delta E^{-1/2}$; and the line sensitivity S_{line} as SNR and $t^{-1/2}$. Therefore, for an observation time, t in seconds, $\Delta E/E$, and continuum, F_{cont} in ph cm−2 s−1 keV−1, or line flux F_{line} in ph cm−2 s−1, we find:

$$\mathrm{SNR(cont)} = 3\left(F_{cont}/\mathrm{S}_{cont}\right)\left(2\Delta E/E\right)^{1/2}\left(t/10^{5}\right)^{1/2}$$

$$\mathrm{SNR(line)} = 3\left(F_{line}/\mathrm{S}_{line}\right)\left(t/10^{6}\right)^{1/2}$$

Recall that if the line is broader than the energy resolution of the instrument, with a FWHM of ΔE, then the signal-to-noise ratio is reduced by $(\Delta E/\delta E)^{1/2}$, where δE is the instrumental FWHM at that energy.

The above back-of-the-envelope calculation is indicative of what can be achieved. For proposals, observer should use the much more accurate on-line Observation Time Estimator (OTE) found on the INTEGRAL web site under *Observation Tools*, as it is the means by which ISOC performs this type of calculation when assessing the technical feasibility of a proposed observation.

Continuum sensitivity values given in earlier are for monochromatic fluxes (ph cm^{-2} s^{-1} keV^{-1}), $\Delta E = E/2$, and can be reliably extrapolated to small energy ranges. However, when ΔE is greater than $E/2$, the energy range must be split into smaller energy bands each with ΔE smaller than $E/2$, in order to calculate the SNR or exposure times in each one, and then combine the results to get the values corresponding to the initial energy range. OTE does this using an input power-law spectral index.

5.2 Sample calculations

5.2.1 Example 1: hard X-ray transient at 100 keV

For a hard transient with a flux of 100 mCrab at 100 keV and a hard power law (photon spectral index Γ of -1) continuum above 100 keV, determine the achievable signal-to-noise ratio at 100 keV in an energy bin corresponding to the instrument FWHM at that energy.

Extrapolating the 2-10 keV flux of the Crab to the γ-ray band with a photon spectral index Γ=-2.1, the flux at 100 keV of a 100 mCrab source is: $F_{cont} = 6.9 \times 10^{-5}$ photons cm^{-2} s^{-1} keV^{-1}.

At this energy, only ISGRI can detect the source because it is below PICsIT's energy range. At 100 keV, ISGRI's energy resolution is $\Delta E/E = 0.08$ (see Figure 11), and its sensitivity is given by Figure 14 and as:

$$S_{cont} = 2.85 \times 10^{-6} \text{ ph cm}^{-2}\text{s}^{-1}\text{ keV}^{-1}$$

If we assume an observation time of 50 ks, $t = 5 \times 10^4$ s, the equation above yields:

$$\text{SNR}_{cont} = 3 \times \left(6.9 \times 10^{-5} / 2.85 \times 10^{-6}\right) \times \left(2 \times 0.08\right)^{-1/2} \times \left(5 \times 10^4 / 10^5\right)^{1/2} = 20.5$$

For these parameters and a 5×5 dither pattern, OTE gives a value of 20σ. Note that OTE also shows that the source is detectable with a significance of 10σ in 13 ks.

5.2.2 Example 2: hard X-ray transient at 800 keV

Consider the same source as in Example 1, but at 800 keV. Extrapolation of the 100 keV flux to 800 keV gives $F_{cont} = 8.5 \times 10^{-6}$ photons cm^{-2} s^{-1} keV^{-1}.

At 800 keV, PICsIT has the higher sensitivity. From Figure 14, and , we find:

$$S_{cont}\,(\text{ISGRI}) = 1.3 \times 10^{-5} \text{ ph cm}^{-2}\text{s}^{-1}\text{ keV}^{-1}$$

$$S_{cont}\,(\text{PICsIT}) = 1.5 \times 10^{-6} \text{ ph cm}^{-2}\text{s}^{-1}\text{ keV}^{-1}$$

Since the sensitivity compared to source flux is lower at 800 keV than at 100 keV, we use a larger energy bin of $\Delta E/E = 0.15$. For the same 50 ks observation time we find:

$$\text{SNR}_{cont}(\text{ISGRI}) = 0.8 \quad \text{and} \quad \text{SNR}_{cont}(\text{PICsIT}) = 6.6$$

For this observation performed with a 5×5 dither, OTE gives 0.8σ and 6.4σ respectively. The source would, therefore, be detected by PICsIT but not by ISGRI. OTE also shows that to detect the source to 10σ, PICsIT needs an exposure time of ~123 ks, whereas ISGRI would require about 8.6 Ms.

5.2.3 Example 3: hard X-ray transient in broad band spectrum

Consider a transient with the same characteristics as the one seen in the previous examples, but for which only the broadband 50–150keV flux is known to be $F_{cont} = 7.6 \times 10^{-5}$ photons cm^{-2} s^{-1} keV^{-1}. For a 50 ks observation, taking a power-law spectrum with $\Gamma = -1$.

In this case, OTE splits the 50-150 keV band into three narrower bands: 50–83 keV, 83–138 keV and 138–150 keV. Table 8 shows the OTE flux, ISGRI sensitivity, and SNR calculated using both Equation 4 (in column 4) and OTE for a 5 × 5 dither (in column 5). Combining in quadrature the SNR values in column 4 to get the 50–150 keV detection significance, we find $\text{SNR}_{cont} = 70$, compared to $\text{SNR}_{cont} = 61$ using the OTE values in column 5, and to $\text{SNR}_{cont} = 80$ if we use the equation in §5.1 (p. 28).

$$\text{SNR}_{cont} = 3 \times \left(7.6 \times 10^{-5} / 2.85 \times 10^{-6}\right) \times \left(2 \times 100/100\right)^{-1/2} \times \left(5 \times 10^4 / 10^5\right)^{1/2} = 80$$

Table 8. OTE example calculation of detection significance in a broad band

Energy band (keV)	Flux (ph cm^{-2} s^{-1} keV^{-1})	Sensitivity (ph cm^{-2} s^{-1} keV^{-1})	SNR	SNR (OTE; 5×5 dither)
50-83	1.06×10^{-4}	5.0×10^{-6}	45	40
83-138	0.64×10^{-4}	2.6×10^{-6}	52	44
138-150	0.48×10^{-4}	3.0×10^{-6}	14	13

5.2.4 Example 4: ^{22}Na line at 1.275 MeV

We are searching for the ^{22}Na line at 1.275 MeV (half life of 3.5 yr) in a bursting transient source. The model-predicted line flux after outburst is: $F_{line} = 10^{-3}$ ph cm^{-2} s^{-1}. The PICsIT line sensitivity given in Figure 14 and is: $S_{line} = 4.8 \times 10^{-4}$ ph cm^{-2} s^{-1}.

For a 500 ks observation, the equation in §5.1 (p. 28) predicts a detection significance of:

$$SNR_{cont} = 3 \times \left(10^{-3}/4.8 \times 10^{-4}\right) \times \left(5 \times 10^{5}/10^{6}\right)^{1/2} = 4.4$$

Similarly, OTE predicts an $SNR_{line} = 4.1$ for such an observation using the 5×5 dither. Moreover, OTE indicates that increasing the detection significance to a value of 10 would require an exposure time of ~3 Ms.